



Article

Dynamic Response of a Light-Modulated Magnetometer to Time-Dependent Fields

Giuseppe Bevilacqua , Valerio Biancalana *  and Yordanka Dancheva † 

DSFTA, Department of Physical Sciences, Earth and Environment, Siena University, Via Roma 56, 53100 Siena, SI, Italy; giuseppe.bevilacqua@unisi.it (G.B.); yordanka.dancheva@aerospazio.com (Y.D.)

* Correspondence: valerio.biancalana@unisi.it

† Current address: Aerospazio Tecnologie S.r.l., Strada di Ficaiole, 53040 Rapolano Terme, SI, Italy.

Abstract: The dynamic response of a Bell-and-Bloom magnetometer to a parallel (to the bias field) time-dependent field is studied by means of a model that goes beyond the commonly assumed quasi-static regime. The findings unveil features that are related to the parametric nature of the considered system. It is shown that for low-amplitude time-dependent fields, different operating conditions are possible and that, besides the commonly reported low-pass filter behavior, a band-pass response emerges. Moreover, we show that a larger amplitude of the time-dependent field makes the parametric nature of the system appear more clearly in the output signal. A harmonic analysis of the latter is numerically performed to highlight and characterize these emerging features.

Keywords: dynamic response; Bell-and-Bloom magnetometer; parametric systems; optical magnetometry

1. Introduction

Resonant magneto-optics and the related field of atomic magnetometry have a history that started in the late 1950s with the research of Dehmelt [1] and Bell and Bloom [2,3] stretching to the 1960s, particularly with the work of Cohen-Tannoudji [4,5]. The following decades brought important progress in the comprehension of optical pumping phenomena [6,7] and prepared the conditions for an important revival at the beginning of the current century [8], which was inspired by numerous attracting applications and facilitated by technological progress.

Most of the application fields envisaged for atomic magnetometers were identified on the basis of their excellent sensitivity, and, in the case of radio-frequency magnetometers, on their response to high-frequency fields. In addition to their use as state-of-the-art detectors in fundamental physics experiments [9], among these application fields emerges the detection of bio-magnetism, e.g., in the construction of magneto-encephalographs [10,11], magneto-cardiographs [12–14], and magneto-miographs [15]. Another promising area is represented by nuclear magnetic resonance in ultra-low (e.g., at microtesla level) or even vanishing fields, where atomic magnetometers find use as non-inductive detectors [16–20], and also in imaging experiments [21–24]. Radio-frequency magnetometers find other interesting applications in the detection and imaging of eddy currents [25,26], with implications in non-destructive testing of materials [27], security [28], and bio-medicine [29]. Further perspectives originate from the possibility of producing miniaturized sensors [30–33] and arranging them in arrays [34].

There exists a variety of atomic magnetometers, which are nowadays also produced as commercial devices. However, they all share several common features [35]. Generally, the working principle consists of using (near) resonant light to orient atoms in a long-lived state (or to induce alignment or higher order momenta); making atoms evolve in the magnetic field under measurement, which thus imprints its features in the subsequent



Citation: Bevilacqua, G.; Biancalana, V.; Dancheva, Y. Dynamic Response of a Light-Modulated Magnetometer to Time-Dependent Fields. *Atoms* **2023**, *11*, 111. <https://doi.org/10.3390/atoms11080111>

Academic Editor: Igor Mykhaylovych Savukov

Received: 5 June 2023

Revised: 2 August 2023

Accepted: 9 August 2023

Published: 11 August 2023



Copyright: © 2023 by the authors. Licensee MDPI, Basel, Switzerland. This article is an open access article distributed under the terms and conditions of the Creative Commons Attribution (CC BY) license (<https://creativecommons.org/licenses/by/4.0/>).

state; and eventually interrogating the atomic sample by means of probe radiation that characterizes its optical (absorptive/dispersive) behavior.

The above mentioned three-step (pumping–evolution–interrogation) procedure [36] can be performed in sequence or simultaneously. Numerous interaction geometries (e.g., the relative orientation of the field, pump beam, and probe beam) can be considered, tailored time-dependent fields can be applied, various approaches (absorption, dispersion, and polarimetry) can be used at the interrogation stage, etc. A *plethora* of configurations can be proposed and this large variety comes with wide ranges of sensitivity, bandwidth, dynamical range, time and space resolution, etc.

An interesting implementation consists of pumping atoms synchronously with their precession around a (nearly) static field. In this case, the pumping radiation must be modulated (in terms of amplitude, polarization, or wavelength) and the probe radiation detects a time-dependent optical behavior. Such a light-modulated setup was firstly proposed by Bell and Bloom [2], who used amplitude-modulated light from a caesium discharge lamp.

The ideal (optimal) configuration of a Bell-and-Bloom setup considers a static magnetic field \mathbf{B} oriented transversely with respect to the pump radiation wave vector. This causes the resonantly induced macroscopic magnetization to precess in a plane perpendicular to \mathbf{B} . This precession can be analyzed by probe radiation propagating in that plane. The Faraday rotation effect offers a favorable detection scheme based on polarimetric measurements; the probe radiation is linearly polarized and the polarization plane is rotated by an angle that oscillates at the precession frequency. The amplitude of this oscillation is maximized when the pumping radiation is modulated at the Larmor frequency set by the static field, i.e., at an atomic magnetic resonance.

If the pump modulation frequency is fixed, small and slow variations in the static field bring the system to a near-resonant condition, with the typical effects of signal reduction and dephasing, the latter being more effectively and easily detected, thanks to its (nearly) linear dependence on the detuning, i.e., on the difference between the frequency at which the pump radiation is modulated and the precession frequency set by the field under measurement.

This classical picture of Bell-and-Bloom behavior applies when the field variation is small compared with the magnetic resonance linewidth and slow with respect to the relaxation time of the atomic orientation. Most of the literature reporting Bell-and-Bloom magnetometers interprets the detected signals in terms of such quasi-static and near-resonant conditions [37], furthermore considering the optimal field orientation. In other terms, the field is usually assumed to be (nearly) perpendicular to the pump and probe propagation, (nearly) time independent, and (nearly) matching the Larmor resonant condition. This paper aims to provide a general analysis of the behavior of a Bell-and-Bloom magnetometer when it operates in the presence of a generic time-dependent field that is parallel to the static (bias) one.

The availability of a more accurate model is of relevance when the output of a magnetometer is used as an error signal to implement feedback-based field stabilization systems [38–42], as well as when designing feed-forward ones [43] or when evaluating the effects of strong stray fields, which is of particular relevance for systems operating in unshielded environments [11,44].

This paper is organized as follows. In Section 2, we describe the mathematical approaches used to solve the Larmor equation under the generic conditions mentioned above. In Section 3, we report the numerical findings of the model, while the main outcomes are discussed in Section 4 and some conclusions are drawn in Section 5.

2. Model

Our aim is to examine the dynamics of spins precessing in a time-dependent magnetic field considering the case of a Bell-and-Bloom magnetometer as sketched in Figure 1. The figure represents a light-modulated magnetometer, in which two laser beams (pump and probe) co-propagate in an atomic vapor in the presence of a time-dependent, trans-

versely oriented magnetic field. The pump beam is modulated and constitutes a time-dependent forcing term that produces a macroscopic magnetization in the medium. This magnetization precesses around the magnetic field and its evolution is detected as a Faraday rotation of the probe beam polarization. A detailed model of the considered spin dynamics enables a more accurate interpretation of the acquired signals. In particular, it helps highlight features that emerge due to the parametric nature of the considered system and that, as we will show, can play a crucial role, particularly in the presence of strong and/or fast varying fields. The starting point in modeling of the spin response is the equation of motion (Larmor equation) for the magnetization vector \mathbf{M} :

$$\dot{\mathbf{M}} = -\Gamma\mathbf{M} + \gamma\mathbf{B}(t) \times \mathbf{M} + \mathbf{f}(t). \tag{1}$$

Here, the constant rate Γ accounts for any relaxation mechanism (assumed isotropic for simplicity), $\mathbf{f}(t)$ is the action of the forcing term obtained through optical pumping (see [45] for details), γ is the gyromagnetic factor, and $\mathbf{B}(t)$ is the applied magnetic field. Finally, $\gamma\mathbf{B}(t) \times \mathbf{M}$ is the magnetic torque experienced by the magnetization vector.

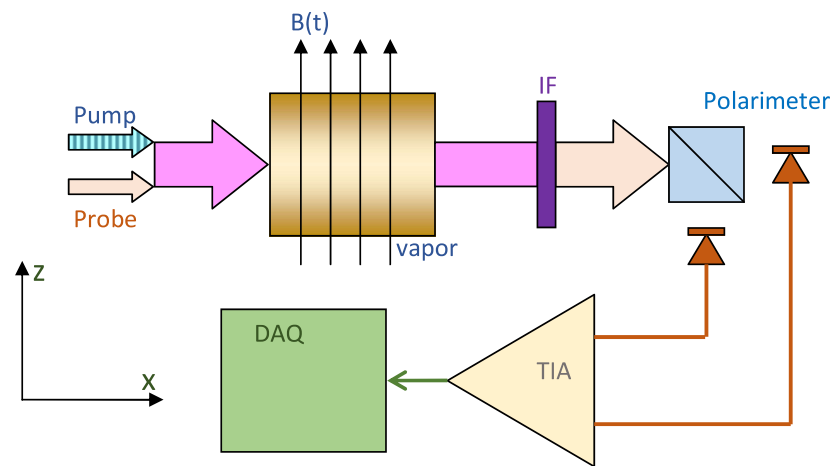


Figure 1. Schematics of a Bell-and-Bloom setup. Two laser beams copropagate in an atomic medium along the x direction in the presence of a transverse time-dependent field oriented along z . The pump beam is modulated in (near) resonance with the spin precession and this causes a macroscopic precessing magnetization. An interference filter (IF) blocks the pump radiation while the probe is polarimetrically analyzed. The polarimeter—made of a polarizing beam splitter, two photo detectors, and a transimpedance amplifier (TIA)—outputs a signal that reproduces the magnetization dynamics and is acquired by an analog-to-digital converter (DAQ) for subsequent numerical elaboration.

In this paper, we are interested in a configuration where the pumping light and the magnetic field are orthogonal. We chose the x axis along the pump (so $\mathbf{f}(t) = f(t)(1, 0, 0)$) and the y axis along the magnetic field, which, in turn, is composed of a static \mathbf{B}_0 and a time-dependent $\mathbf{B}_{\parallel}(t)$ part. Introducing the frequencies $\omega_0 = \gamma B_0$ and $\omega_{\parallel} = \gamma B_{\parallel}$, the relevant Larmor equation becomes

$$\dot{W} = -\Gamma W - i(\omega_0 + \omega_{\parallel}(t))W + f(t), \tag{2}$$

where $W = M_x + iM_z$, and we are interested in $M_x = \text{Re}(W)$, which is the quantity related to the Faraday rotation of the probe laser collinear with the pump as, for example, in [45,46].

The solution of (2), which is a first-order, linear, non-homogeneous, and parametric differential equation, can be written as

$$W(t) = e^{-\Gamma t - i\omega_0 t - i\theta_{\parallel}(t)} W(0) + e^{-\Gamma t - i\omega_0 t - i\theta_{\parallel}(t)} \int_0^t dt' e^{\Gamma t' + i\omega_0 t' + i\theta_{\parallel}(t')} f(t'), \tag{3}$$

where we introduce the Larmor angle associated with the time-dependent field:

$$\theta_{\parallel}(t) = \int_0^t \omega_{\parallel}(s) \, ds. \tag{4}$$

We assume that both the forcing and the time-dependent field are real-valued periodic functions that can be expressed in terms of Fourier series. Namely, we assume that the forcing term oscillates with period $T_{\text{forcing}} = 2\pi/\Omega$ and the time-dependent field oscillates with period $T_{\text{field}} = 2\pi/\omega$:

$$f(t) = \sum_{n=-\infty}^{+\infty} f_n e^{in\Omega t} \quad f_{-n} = f_n^* \tag{5a}$$

$$\omega_{\parallel}(t) = \sum_{n=-\infty}^{+\infty} x_n e^{in\omega t} \quad x_{-n} = x_n^* \tag{5b}$$

and we can set $x_0 = 0$ (or otherwise redefine ω_0), obtaining that θ_{\parallel} is also a periodic function, which permits us to write

$$e^{i\theta_{\parallel}(t)} = \sum_{n=-\infty}^{+\infty} G_n e^{in\omega t} \quad e^{-i\theta_{\parallel}(t)} = \sum_{n=-\infty}^{+\infty} G_{-n}^* e^{in\omega t}, \tag{6}$$

where the G_n coefficients are complicated functions of $x_n/n\omega$. It is worth noting that the G_n coefficients are related to the Bessel functions of the first kind in the case of a purely sinusoidal time-dependent field.

Now, the steady-state (SS) solution, valid for $t \gg 1/\Gamma$, of (3) becomes

$$W(t) = e^{-i\theta_{\parallel}(t)} \sum_{n,m} \frac{G_n f_m}{\Gamma + i(\omega_0 + n\omega + m\Omega)} e^{i(n\omega + m\Omega)t}, \tag{7}$$

which can be simplified by taking into account that, under usual experimental conditions, the pumping frequency is (nearly) resonant with the Larmor frequency set by the static field, that is, $\Omega \approx \omega_0$, resulting in

$$\begin{aligned} W(t) &\approx e^{-i\theta_{\parallel}(t)} \sum_n \frac{f_{-1} G_n e^{in\omega t}}{\Gamma + i(\omega_0 - \Omega + n\omega)} e^{-i\Omega t} \\ &= \sum_s \sum_n \frac{f_{-1} G_n G_{n-s}^* e^{is\omega t}}{\Gamma + i\delta + in\omega} e^{-i\Omega t} \\ &\equiv \sum_s Z_s e^{is\omega t} e^{-i\Omega t} \\ &\equiv Z(t) e^{-i\Omega t}, \end{aligned} \tag{8}$$

where we introduced the detuning $\delta = \omega_0 - \Omega$ and implicitly defined the Z_s coefficients and the $Z(t)$ complex function.

We would like to point out that result (8) has a more general validity; indeed, it is valid also when the experimental apparatus tracks the component at the fundamental frequency of the pumping modulation. In fact, in this case, the approximation is valid just because this is the term singled out by the measuring apparatus. The validity of the approximation in the resonant case ($\Omega \approx \omega_0$) comes from the fact that the singled out term is the biggest one in the sum over m .

After this demodulation, the quantity monitored is the phase of $Z(t)$, which is still a periodic function:

$$\varphi(t) \equiv \arg(Z(t)) = \text{Im}(\log(Z(t))) = \sum_n \varphi_n e^{in\omega t} \quad \varphi_{-n} = \varphi_n^*, \tag{9}$$

where, in general, the φ_n coefficients can be evaluated only numerically as

$$\varphi_n = \frac{1}{2\pi} \int_0^{2\pi} e^{-in\theta} \arg\left(\sum_s Z_s e^{is\theta}\right) d\theta. \tag{10}$$

A notable exception is the case of a low-intensity time-dependent field which is discussed in the following.

Low-Intensity Limit

When the time-dependent field is small with respect to the static one, which in our formalism means that the x_n coefficients are small quantities, i.e., $x_n \rightarrow \epsilon x_n$, where ϵ is a small positive quantity, the Larmor angle becomes $\epsilon\theta_{\parallel}$, a small quantity too. It follows that $e^{i\epsilon\theta_{\parallel}} = 1 + i\epsilon\theta_{\parallel} + O(\epsilon^2)$ and $G_0 = 1 - \epsilon \sum_n (x_n/n\omega) + O(\epsilon^2)$, $G_n = \epsilon x_n/n\omega + O(\epsilon^2)$ for $n \neq 0$. Substituting this in the first line of (8), one obtains

$$\begin{aligned} Z(t) &= e^{-i\theta_{\parallel}} f_{-1} \left[\frac{G_0}{\Gamma + i\delta} + \sum_{n \neq 0} \frac{G_n}{\Gamma + i\delta + in\omega} e^{in\omega t} \right] \\ &= e^{-i\epsilon\theta_{\parallel}} \frac{f_{-1}}{\Gamma + i\delta} \left[1 - \epsilon \sum_n \frac{x_n}{n\omega} + \epsilon \sum_{n \neq 0} \frac{x_n}{n\omega} \left(1 - \frac{in\omega}{\Gamma + i\delta + in\omega} \right) e^{in\omega t} + O(\epsilon^2) \right] \\ &= e^{-i\epsilon\theta_{\parallel}} \frac{f_{-1}}{\Gamma + i\delta} \left[1 + \epsilon \sum_n \frac{x_n}{n\omega} (e^{in\omega t} - 1) - i\epsilon \sum_n \frac{x_n}{\Gamma + i\delta + in\omega} e^{in\omega t} + O(\epsilon^2) \right]. \end{aligned}$$

Considering that the second term in parentheses is $i\epsilon\theta_{\parallel}$ and that $\log(1 + \epsilon X) = \epsilon X + O(\epsilon^2)$ for small ϵ , one obtains for the phase $\varphi(t)$:

$$\varphi(t) = \arg\left(\frac{f_{-1}}{\Gamma + i\delta}\right) - \epsilon \operatorname{Im}\left(i \sum_n \frac{x_n}{\Gamma + i\delta + in\omega} e^{in\omega t}\right) + O(\epsilon^2). \tag{11}$$

Here, the first term is just a constant offset which depends also, through the coefficient f_{-1} , on the precise characteristics of the pump modulation signal. We disregard this term because it does not contain information about the dynamical field encoded in the x_n coefficients. The next term, the first order in ϵ in this perturbation theory, contains relevant information, and after some algebra, can be rewritten as

$$\varphi^{\text{pert}}(t) \equiv -\frac{1}{2} \sum_n \left(\frac{1}{\Gamma + i\delta + in\omega} + \frac{1}{\Gamma - i\delta + in\omega} \right) x_n e^{in\omega t}, \tag{12}$$

which is identical to the expression reported in [47] and can be recast as the output of a linear system

$$\varphi^{\text{pert}}(t) = - \int_0^t e^{-\Gamma(t-t')} \cos(\delta(t-t')) \omega_{\parallel}(t') dt'. \tag{13}$$

3. Results

The result reported in (8) is quite general and applies to a complicated time dependence of ω_{\parallel} which would require the consideration of many x_n parameters, as well as of the case of a simple sinusoidal oscillation.

It is worth to point out that in the phase time signal (Equation (9)), the coefficient f_{-1} gives only a constant contribution which amounts to an experimental offset and can be safely neglected, resulting in an experimental advantage because one does not need to take into account the precise form of the pumping signal. This is not the case if one chooses to

monitor the modulus of $Z(t)$, where the f_{-1} coefficient enters in a multiplicative way. This can be seen by inspection, noting that $Z(t)$ can be rewritten as $Z(t) = f_{-1}\bar{Z}(t)$ and then

$$|Z(t)| = |f_{-1}||\bar{Z}(t)| \tag{14a}$$

$$\varphi(t) = \text{Im} \log(f_{-1}) + \text{Im} \log(\bar{Z}(t)) \tag{14b}$$

As a result of the complicated dependence of the G_n coefficients on x_n , it is difficult to draw valid conclusions for arbitrary values of the parameters. In such a sense, the analytical low-intensity limit of Equation (12) is a nice result, which allows a discussion in terms of linear time-invariant systems. However, in this paper, we explore the complementary regime, presenting results obtained as explained in the previous section.

To be more concrete, we fix the time dependence as a simple cosine, namely, $\omega_{\parallel} = \Omega_{\parallel} \cos(\omega t)$, so that $G_n \equiv J_n(\Omega_{\parallel}/\omega)$ are the Bessel functions of first kind and the coefficients Z_s can be written as

$$Z_s = f_{-1} \sum_n \frac{J_n J_{n-s}}{\Gamma + i\delta + i n \omega} \tag{15}$$

and we expect that for not-so-small Ω_{\parallel} , the higher-harmonic coefficients φ_n ($n > 1$) will also become important. In fact, the system is a parametric one and it will show a kind of “non-linear” behavior. In other terms, even for a simple sinusoidal time-dependent field as “input”, higher order harmonics will appear in the monitored phase.

In the following pictures, we present numerical results for the first Fourier coefficients of the phase for different values of the amplitude of the time-dependent field. The reported simulations use only adimensional parameters to simplify as much as possible the physical discussion and to make the plots applicable to systems characterized by diverse values of Γ . We choose to use Γ as the relevant frequency scale.

In Figures 2–5, the modulus of φ_n $n = 1, 2, 3$ (from left to right) is reported as a function of ω for fixed values of $\Omega_{\parallel}/\Gamma = 0.1, 0.5, 1.0, 2.0$, respectively. Each curve represents a different value of the detuning δ in units of Γ .

As can be seen in Figure 2, where $\Omega_{\parallel} = 0.1 \Gamma$, the perturbative limit of Equation (13) applies. In fact, φ_2 and φ_3 are two and three orders of magnitude smaller than φ_1 , respectively. However, as can be seen in Figures 3–5, φ_2 and φ_3 become increasingly comparable in magnitude with φ_1 when the amplitude Ω_{\parallel} of the time-dependent field is increased.

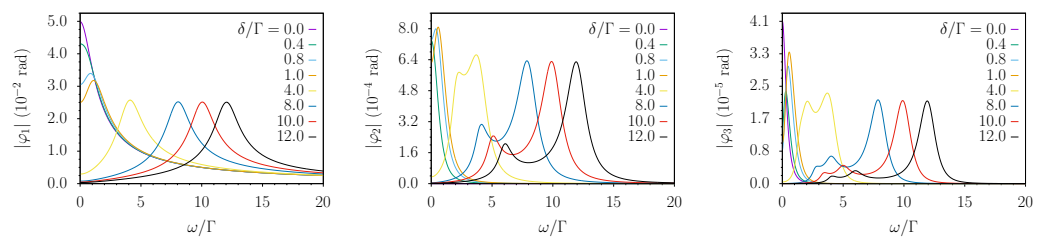


Figure 2. The modulus of the first Fourier coefficients of the phase for $\Omega_{\parallel} = 0.1 \Gamma$. From left to right: $|\varphi_1|$, $|\varphi_2|$, and $|\varphi_3|$.

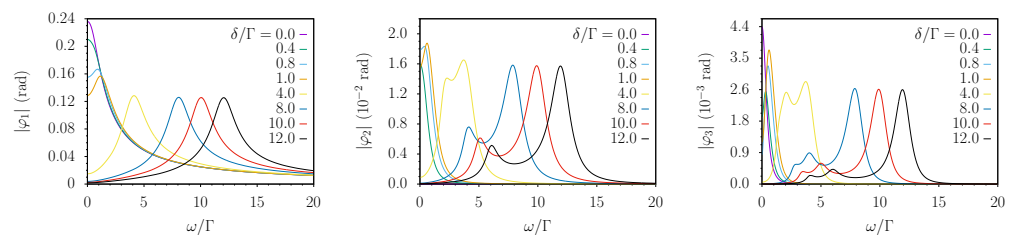


Figure 3. The modulus of the first Fourier coefficients of the phase for $\Omega_{\parallel} = 0.5 \Gamma$. From left to right: $|\varphi_1|$, $|\varphi_2|$, and $|\varphi_3|$.

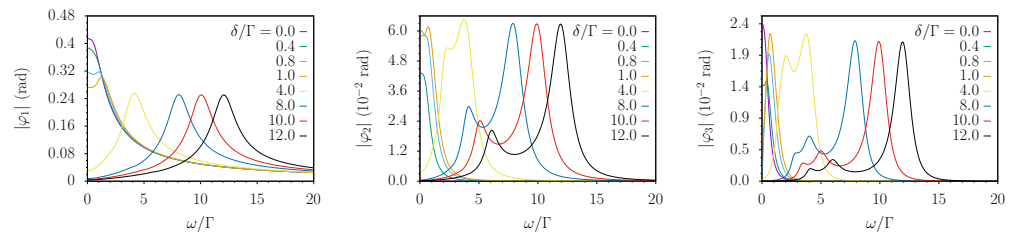


Figure 4. The modulus of the first Fourier coefficients of the phase for $\Omega_{\parallel} = 1.0\Gamma$. From left to right: $|\varphi_1|$, $|\varphi_2|$, and $|\varphi_3|$.

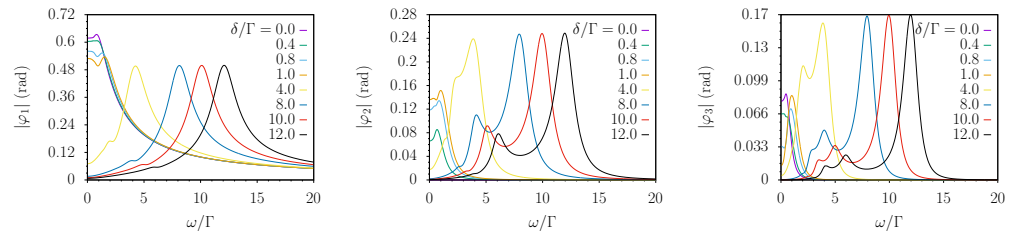


Figure 5. The modulus of the first Fourier coefficients of the phase for $\Omega_{\parallel} = 2.0\Gamma$. From left to right: $|\varphi_1|$, $|\varphi_2|$, and $|\varphi_3|$.

Let us consider the behavior of φ_1 for different values of δ/Γ . For small δ/Γ , the curve can be interpreted as the response of a low-pass filter, while when increasing δ/Γ it resembles a band-pass filter centered in $\omega \approx \delta$. This point of view is reinforced in the low Ω_{\parallel} regime by the result of Equation (13). However, as can be seen in the pictures, this interpretation can be pushed also for higher values of Ω_{\parallel} even if some structure starts appearing close to $\omega \approx \delta/2$.

The behavior of φ_2 is more structured. For $\delta/\Gamma = 0$ (we observed this for all the even coefficients φ_{2n}), a “low-pass” profile evolves into a double peaked structure with the highest peak centered around $\omega \approx \delta$ and the other around $\omega \approx \delta/2$. Increasing Ω_{\parallel} gives rise to a small structure close to $\omega \approx \delta/3$.

Similar conclusions can be drawn for φ_3 ; here, the number of visible peaks is three even for small Ω_{\parallel} . It seems reasonable to assume that this is the general behavior of the coefficients φ_n , i.e., increasing Ω_{\parallel} increases both the number of “relevant” φ_n and for each φ_n the number of visible peaks are centered at $\omega \approx \delta/k$.

An alternative and complementary visualization of the described phenomenology is reported in Figures 6 and 7. In these maps, the modulus of the signals at ω , 2ω , and 3ω (from left to right) is mapped as a function of the frequency (horizontal axes) and amplitude (vertical axes) of the time-dependent field. The two figures refer to cases of small detuning (low pass behavior) and large detuning (band pass behavior), respectively.

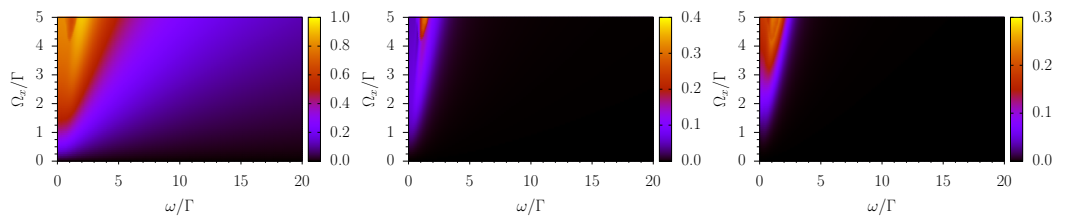


Figure 6. Maps of the modulus of the first Fourier coefficients of the phase for $\delta = 0.4\Gamma$. From left to right: $|\varphi_1|$, $|\varphi_2|$, and $|\varphi_3|$.

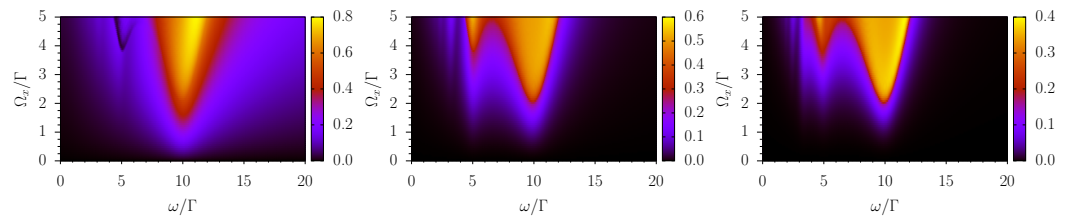


Figure 7. Maps of the modulus of the first Fourier coefficients of the phase for $\delta = 10\Gamma$. From left to right: $|\varphi_1|$, $|\varphi_2|$, and $|\varphi_3|$.

4. Discussion

The main scope of this paper is to investigate the dynamic response of a Bell-and-Bloom system to a time-dependent field parallel to the bias one. This subject is often presented in terms of an approximation, the validity of which requires that the time-dependent field is small and varies slowly with respect to relaxation time and that the pumping radiation is modulated in resonance with the precession frequency set by the dominant static field. Under these stringent but frequently fulfilled conditions, the systems permits a simplified treatment and behaves as a linear forced-damped oscillator with a low-pass (Butterworth filter) response [10,48].

We have previously analyzed the behavior of such a system using a perturbative approach in the amplitude of the time-dependent field [47] in a more general configuration, as a generic orientation of the field was considered. Before discussing the results presented in Section 3, it is worth recalling the main outcomes obtained with that approach.

Apart from the basic physical interest to characterize and model spin dynamics in a time-dependent field, our study can help interpret the recorded magnetometric signals more accurately. In particular, it provides a quantitative evaluation of the harmonic distortion that occurs with increasing field variations and allows us to evaluate the distortions in the time domain caused by a frequency-dependent signal phase shift. The latter is particularly relevant when the magnetic signals contain broad spectrum characteristics, as in the case of traces with sharp edges or spikes.

4.1. Perturbative Results

An interesting feature resulting from the first-order perturbative approximation emerges when the pump radiation is modulated at a frequency detuned from the exact resonance. Under this condition, the simplified low-pass response becomes inadequate and a band-pass behavior is observed, with an enhanced response to AC components at frequencies close to the pump frequency detuning δ , as also observed in ref. [42].

In application, this feature may help tailor the system response to the detection of oscillating terms at frequencies around δ . For instance, a magnetometer with a resonance as narrow as 20 Hz maybe used to detect an AC field oscillating at 200 Hz with a good efficiency, provided that the pump light is modulated at a frequency 200 Hz away from γB_{DC} .

An interesting behavior is obtained at an intermediate detuning, $\delta \approx \Gamma/2$. This condition produces a nearly flat amplitude response up to a cut-off frequency set by $\Gamma/2$. Such an extended flat bandwidth is obtained at the expense of a slight reduction in the signal amplitude, if compared to the $\delta = 0$ case. Concerning the phase of the magnetometric signal, a maximally extended constant phase (non dispersive) response is instead achieved under the condition $\delta = \Gamma$.

In this first-order approximation, the precessing spins do not respond to field variations along direction perpendicular to the static field; such a response appears in the next order. Indeed, the perturbative treatment developed in [47] shows that the second-order approximation predicts terms that *double* and *mix* the frequencies at which time-dependent fields are applied. It is worth noting that frequency mixing among diverse components of the time-dependent field comes with several peculiar features and it does not occur among all the couples of components, as detailed in [47].

A further increase in the time-dependent field also makes the second-order approximation inadequate and the numerical analysis developed in Section 2 becomes necessary. For the sake of simplicity, in this work, the time-dependent field is considered at arbitrarily high amplitudes, but only along the bias field direction. Moreover, the presented results are obtained with a single-frequency term, so that no frequency mixing occurs and the non-linearities are pointed out in terms of a harmonic analysis.

4.2. Non-Perturbative Results

The numerical analysis performed at a rather weak intensity is perfectly consistent with the first-order perturbative analysis recalled in Section 4.1. In particular, the leftmost plot in Figure 2 shows that at resonance ($\delta = 0$), the system has a low-pass response, which evolves into an extended flat response when $\delta \approx \Gamma$ and becomes a band-pass one for $\delta > \Gamma$. At large detunings (band-pass regime), the peak response is half the maximum observed at low frequency and vanishing detunings. A harmonic analysis shows that in the low-field regime ($\Omega_{\parallel} \ll \Gamma$), the anharmonicity of the response is negligible. A close inspection of the vertical scales in Figure 2 highlights that the second and third harmonic terms (φ_2, φ_3) are depressed by two and three order of magnitudes with respect to the fundamental one, respectively.

Figures 3 and 4 show the effects of a moderate increase in the amplitude of the time-dependent field. Under conditions in which $\Omega_{\parallel} \approx \Gamma$, the low-pass and band-pass behavior does not change appreciably, while the anharmonicity becomes progressively more evident, e.g., for $\Omega_{\parallel} = \Gamma$, the third harmonic peaks observed at large detunings are only one order of magnitude weaker than the fundamental one.

The results obtained at small and moderate amplitudes of the time-dependent field (Figures 2–4) show pretty similar features in the spectral response, and the main difference concerns only the anharmonicity level. The response observed for large δ/Γ is characterized by a peak at $\omega \approx \delta$ for all harmonic terms. However, the second harmonic term (φ_2) also has a secondary peak at $\omega \approx \delta/2$ and an additional peak at $\omega \approx \delta/3$ emerges for the third harmonic term, φ_3 .

Figure 5 shows new spectral features in the responses. Strong time-dependent fields cause extra peaks to emerge in the plots. In particular, the leftmost plot (φ_1) of Figure 5 shows the appearance of an extra peak at $\omega \approx \delta/2$.

The maps shown in Figures 6 and 7 confirm the analysis reported above. In these figures, it can be seen that the amplitudes of higher harmonics (φ_2 and φ_3) become comparable to that of the fundamental tone φ_1 for large values of Ω_x ($\Omega_x \gtrsim \Gamma$), and that they have a more structured dependence on ω . In addition, it can be observed that both the fundamental tone and the higher harmonics peak at $\omega \approx \delta$ and that secondary peaks appear at sub-harmonics in the case of φ_2 and φ_3 .

5. Conclusions

We studied the effect of a time-dependent magnetic field on the Bell-and-Bloom magnetometer in the configuration in which the time-dependent magnetic field is parallel to the bias static one. We generalized the analysis beyond the quasi-static and low-amplitude regime usually found in the literature, unveiling interesting features such as confirming the low-pass to band-pass transition for a large amplitude of the time-dependent field. Moreover, for large amplitudes of the time-dependent field, the emergence of the “non-linear” behavior of the system is demonstrated.

Our findings may be of interest to improve the accuracy of the interpretation of magnetometric measurements, in particular to evaluate their harmonic distortion, and to better reconstruct magnetic signals characterized by relatively broad spectra. The analysis of the response to large field variations covers a phenomenology that is normally overlooked in applied research, as the latter is often focused on the detection of weak signals. Furthermore, it highlights and characterizes the non-linear features that can contaminate the measurement when strong stray field disturbances are superimposed on the weak signals

under investigation. An interesting outcome consists of a feature that is observed when the detuning is progressively increased; correspondingly, the response of the system evolves from the well-known low-pass behavior to band-pass behavior. This latter can be of great relevance, for instance, when noise spectra are experimentally recorded to evaluate system performance and specifically sensitivity profiles.

Author Contributions: Conceptualization, G.B., V.B. and Y.D.; methodology, G.B.; software, G.B.; validation, G.B., V.B. and Y.D.; formal analysis, G.B.; investigation, G.B., V.B. and Y.D.; data curation, G.B.; writing—original draft preparation, G.B. and V.B.; writing—review and editing, G.B., V.B. and Y.D.; visualization, G.B. All authors have read and agreed to the published version of the manuscript.

Funding: This research received no external funding.

Data Availability Statement: Data are contained within the article in a graphical form. Numerical data are available on reasonable request from the corresponding author.

Acknowledgments: G.B. is partially supported by the GNFM of Indam.

Conflicts of Interest: The authors declare no conflict of interest.

References

1. Dehmelt, H.G. Modulation of a Light Beam by Precessing Absorbing Atoms. *Phys. Rev.* **1957**, *105*, 1924–1925. [[CrossRef](#)]
2. Bell, W.E.; Bloom, A.L. Optical Detection of Magnetic Resonance in Alkali Metal Vapor. *Phys. Rev.* **1957**, *107*, 1559–1565. [[CrossRef](#)]
3. Bell, W.E.; Bloom, A.L. Optically Driven Spin Precession. *Phys. Rev. Lett.* **1961**, *6*, 280–281. [[CrossRef](#)]
4. Dupont-Roc, J. Détermination par des méthodes optiques des trois composantes d'un champ magnétique très faible. *Rev. Phys. Appl.* **1970**, *5*, 853–864. [[CrossRef](#)]
5. Dupont-Roc, J.; Haroche, S.; Cohen-Tannoudji, C. Detection of very weak magnetic fields (10^{-9} gauss) by ^{87}Rb zero-field level crossing resonances. *Phys. Lett. A* **1969**, *28*, 638–639. [[CrossRef](#)]
6. Happer, W. Optical Pumping. *Rev. Mod. Phys.* **1972**, *44*, 169–249. [[CrossRef](#)]
7. Happer, W.; Jau, Y.; Walker, T. Optical Pumping of Atoms. In *Optically Pumped Atoms*; Wiley VCH Verlag GmbH & Co. KGaA: Weinheim, Germany, 2010; Chapter 5, pp. 49–71. [[CrossRef](#)]
8. Budker, D.; Romalis, M. Optical magnetometry. *Nat. Phys.* **2007**, *3*, 227–234. [[CrossRef](#)]
9. Afach, S.; Aybas Turturk, D.; Bekker, H.; Buchler, B.C.; Budker, D.; Cervantes, K.; Derevianko, A.; Eby, J.; Figueroa, N.L.; Folman, R.; et al. What Can a GNOME Do? Search Targets for the Global Network of Optical Magnetometers for Exotic Physics Searches. *Ann. Der Phys.* **2003**, *2003*, 2300083. [[CrossRef](#)]
10. Colombo, A.P.; Carter, T.R.; Borna, A.; Jau, Y.Y.; Johnson, C.N.; Dagel, A.L.; Schwindt, P.D.D. Four-channel optically pumped atomic magnetometer for magnetoencephalography. *Opt. Express* **2016**, *24*, 15403–15416. [[CrossRef](#)] [[PubMed](#)]
11. Wu, T.; Peng, X.; Chen, J.; Guo, H. Fiber-Coupled OPM in Purely Coil-Shielded Environment. In *Flexible High Performance Magnetic Field Sensors: On-Scalp Magnetoencephalography and Other Applications*; Labyt, E., Sander, T., Wakai, R., Eds.; Springer International Publishing: Cham, Switzerland, 2022; pp. 161–177. [[CrossRef](#)]
12. Bison, G.; Castagna, N.; Hofer, A.; Knowles, P.; Schenker, J.L.; Kasprzak, M.; Saudan, H.; Weis, A. A room temperature 19-channel magnetic field mapping device for cardiac signals. *Appl. Phys. Lett.* **2009**, *95*, 173701. [[CrossRef](#)]
13. Kamada, K.; Ito, Y.; Kobayashi, T. Human MCG measurements with a high-sensitivity potassium atomic magnetometer. *Physiol. Meas.* **2012**, *33*, 1063. [[CrossRef](#)]
14. Kim, Y.J.; Savukov, I.; Newman, S. Magnetocardiography with a 16-channel fiber-coupled single-cell Rb optically pumped magnetometer. *Appl. Phys. Lett.* **2019**, *114*, 143702. [[CrossRef](#)]
15. Broser, P.J.; Knappe, S.; Kajal, D.S.; Noury, N.; Alem, O.; Shah, V.; Braun, C. Optically Pumped Magnetometers for Magneto-Myography to Study the Innervation of the Hand. *IEEE Trans. Neural. Syst. Rehabil. Eng.* **2018**, *26*, 2226–2232. [[CrossRef](#)] [[PubMed](#)]
16. Savukov, I.M.; Romalis, M.V. NMR Detection with an Atomic Magnetometer. *Phys. Rev. Lett.* **2005**, *94*, 123001. [[CrossRef](#)]
17. Bevilacqua, G.; Biancalana, V.; Dancheva, Y.; Vigilante, A.; Donati, A.; Rossi, C. Simultaneous Detection of H and D NMR Signals in a micro-Tesla Field. *J. Phys. Chem. Lett.* **2017**, *8*, 6176–6179. [[CrossRef](#)]
18. Tayler, M.C.; Gladden, L.F. Scalar relaxation of NMR transitions at ultralow magnetic field. *J. Magn. Reson.* **2019**, *298*, 101–106. [[CrossRef](#)] [[PubMed](#)]

19. Savukov, I.; Kim, Y.J.; Schultz, G. Detection of ultra-low field NMR signal with a commercial QuSpin single-beam atomic magnetometer. *J. Magn. Reson.* **2020**, *317*, 106780. [[CrossRef](#)] [[PubMed](#)]
20. Eills, J.; Cavallari, E.; Carrera, C.; Budker, D.; Aime, S.; Reineri, F. Real-Time Nuclear Magnetic Resonance Detection of Fumarase Activity Using Parahydrogen-Hyperpolarized [1-(13)C]Fumarate. *J. Am. Chem. Soc.* **2019**, *80*, 20209–20214. [[CrossRef](#)]
21. Savukov, I.; Karaulanov, T. Magnetic-resonance imaging of the human brain with an atomic magnetometer. *Appl. Phys. Lett.* **2013**, *103*, 043703. [[CrossRef](#)]
22. Savukov, I.; Karaulanov, T. Anatomical MRI with an atomic magnetometer. *J. Magn. Reson.* **2013**, *231*, 39–45. [[CrossRef](#)]
23. Bevilacqua, G.; Biancalana, V.; Dancheva, Y.; Vigilante, A. Restoring Narrow Linewidth to a Gradient-Broadened Magnetic Resonance by Inhomogeneous Dressing. *Phys. Rev. Appl.* **2019**, *11*, 024049. [[CrossRef](#)]
24. Bevilacqua, G.; Biancalana, V.; Dancheva, Y.; Vigilante, A. Sub-millimetric ultra-low-field MRI detected in situ by a dressed atomic magnetometer. *Appl. Phys. Lett.* **2019**, *115*, 174102. [[CrossRef](#)]
25. Deans, C.; Marmugi, L.; Hussain, S.; Renzoni, F. Electromagnetic induction imaging with a radio-frequency atomic magnetometer. *Appl. Phys. Lett.* **2016**, *108*, 103503. [[CrossRef](#)]
26. Bevington, P.; Gartman, R.; Chalupczak, W. Object detection with an alkali-metal spin maser. *J. Appl. Phys.* **2021**, *130*, 214501. [[CrossRef](#)]
27. Bevington, P.; Gartman, R.; Chalupczak, W.; Deans, C.; Marmugi, L.; Renzoni, F. Non-destructive structural imaging of steelwork with atomic magnetometers. *Appl. Phys. Lett.* **2018**, *113*, 063503. [[CrossRef](#)]
28. Darrer, B.J.; Watson, J.C.; Bartlett, P.; Renzoni, F. Magnetic Imaging: A New Tool for UK National Nuclear Security. *Sci. Rep.* **2015**, *5*, 7944. [[CrossRef](#)]
29. Marmugi, L.; Renzoni, F. Optical Magnetic Induction Tomography of the Heart. *Sci. Rep.* **2016**, *6*, 23962. [[CrossRef](#)] [[PubMed](#)]
30. Gerginov, V.; Pomponio, M.; Knappe, S. Scalar Magnetometry Below 100 fT/Hz^{1/2} in a Microfabricated Cell. *IEEE Sens. J.* **2020**, *20*, 12684–12690. [[CrossRef](#)]
31. Scholtes, T.; Woetzel, S.; IJsselsteijn, R.; Schultze, V.; Meyer, H.G. Intrinsic relaxation rates of polarized Cs vapor in miniaturized cells. *Appl. Phys. B* **2014**, *117*, 211–218. [[CrossRef](#)]
32. Zhang, Y.; Tian, Y.; Li, S.; Chen, J.; Gu, S. Faraday-Rotation Atomic Magnetometer Using Triple-Chromatic Laser Beam. *Phys. Rev. Appl.* **2019**, *12*, 011004. [[CrossRef](#)]
33. Li, S.; Zhang, Y.; Tian, Y.; Chen, J.; Gu, S. Faraday-rotation Bell–Bloom atomic magnetometer using an alternating pump–probe beam. *J. Appl. Phys.* **2021**, *130*, 084501. [[CrossRef](#)]
34. Nardelli, N.V.; Perry, A.R.; Krzyzewski, S.P.; Knappe, S.A. A conformal array of microfabricated optically-pumped first-order gradiometers for magnetoencephalography. *EPJ Quantum Technol.* **2014**, *7*, 11. [[CrossRef](#)]
35. Fabricant, A.; Novikova, I.; Bison, G. How to build a magnetometer with thermal atomic vapor: A tutorial. *New J. Phys.* **2023**, *25*, 025001. [[CrossRef](#)]
36. Weis, A.; Bison, G.; Pazgalev, A.S. Theory of double resonance magnetometers based on atomic alignment. *Phys. Rev. A* **2006**, *74*, 033401. [[CrossRef](#)]
37. Zhang, R.; Wu, T.; Chen, J.; Peng, X.; Guo, H. Frequency Response of Optically Pumped Magnetometer with Nonlinear Zeeman Effect. *Appl. Sci.* **2020**, *10*, 7031. [[CrossRef](#)]
38. Li, S.; Liu, J.; Jin, M.; Tetteh Akiti, K.; Dai, P.; Xu, Z.; Eric-Theophilus Nwodom, T. A kilohertz bandwidth and sensitive scalar atomic magnetometer using an optical multipass cell. *Measurement* **2022**, *190*, 110704. [[CrossRef](#)]
39. Bevilacqua, G.; Biancalana, V.; Dancheva, Y.; Vigilante, A. Self-Adaptive Loop for External-Disturbance Reduction in a Differential Measurement Setup. *Phys. Rev. Appl.* **2019**, *11*, 014029. [[CrossRef](#)]
40. Pyragius, T.; Jensen, K. A high performance active noise control system for magnetic fields. *Rev. Sci. Instrum.* **2021**, *92*, 124702. [[CrossRef](#)]
41. Yan, Y.; Lu, J.; Zhang, S.; Lu, F.; Yin, K.; Wang, K.; Zhou, B.; Liu, G. Three-axis closed-loop optically pumped magnetometer operated in the SERF regime. *Opt. Express* **2022**, *30*, 18300–18309. [[CrossRef](#)]
42. Ding, Y.; Xiao, W.; Zhao, Y.; Wu, T.; Peng, X.; Guo, H. Dual-Species All-Optical Magnetometer Based on a Cs-K Hybrid Vapor Cell. *Phys. Rev. Appl.* **2023**, *19*, 034066. [[CrossRef](#)]
43. O'Dwyer, C.; Ingleby, S.J.; Chalmers, I.C.; Griffin, P.F.; Riis, E. A feed-forward measurement scheme for periodic noise suppression in atomic magnetometry. *Rev. Sci. Instrum.* **2020**, *91*, 045103. [[CrossRef](#)] [[PubMed](#)]
44. Cooper, R.J.; Prescott, D.W.; Lee, G.J.; Sauer, K.L. RF atomic magnetometer array with over 40 dB interference suppression using electron spin resonance. *J. Magn. Reson.* **2018**, *296*, 36–46. [[CrossRef](#)] [[PubMed](#)]
45. Bevilacqua, G.; Biancalana, V.; Dancheva, Y. Atomic orientation driven by broadly-frequency-modulated radiation: Theory and experiment. *Phys. Rev. A* **2016**, *94*, 012501. [[CrossRef](#)]
46. Bevilacqua, G.; Biancalana, V.; Chessa, P.; Dancheva, Y. Multichannel optical atomic magnetometer operating in unshielded environment. *Appl. Phys. B* **2016**, *122*, 103. [[CrossRef](#)]

47. Bevilacqua, G.; Biancalana, V.; Dancheva, Y.; Fregosi, A.; Vigilante, A. Spin dynamic response to a time dependent field. *Appl. Phys. B* **2021**, *127*, 128. [[CrossRef](#)]
48. Zhang, R.; Pang, B.; Li, W.; Yang, Y.; Chen, J.; Peng, X.; Guo, H. Frequency Response of a Close-Loop Bell-Bloom Magnetometer. In Proceedings of the 2018 IEEE International Frequency Control Symposium (IFCS), Olympic Valley, CA, USA, 21–24 May 2018; pp. 1–3. [[CrossRef](#)]

Disclaimer/Publisher’s Note: The statements, opinions and data contained in all publications are solely those of the individual author(s) and contributor(s) and not of MDPI and/or the editor(s). MDPI and/or the editor(s) disclaim responsibility for any injury to people or property resulting from any ideas, methods, instructions or products referred to in the content.